ISSN 0036-0236, Russian Journal of Inorganic Chemistry, 2019, Vol. 64, No. 3, pp. 296–302. © Pleiades Publishing, Ltd., 2019.
Russian Text © E.A. Potanina, A.I. Orlova, A.V. Nokhrin, D.A. Mikhailov, M.S. Boldin, N.V. Sakharov, O.A. Belkin, E.A. Lantsev, M.G. Tokarev, V.N. Chuvil'deev, 2019, published in Zhurnal Neorganicheskoi Khimii, 2019, Vol. 64, No. 3, pp. 243–250.

SYNTHESIS AND PROPERTIES OF INORGANIC COMPOUNDS

Fine-Grained Tungstates $SrWO_4$ and $NaNd(WO_4)_2$ with the Scheelite Structure Prepared by Spark Plasma Sintering

E. A. Potanina[a], *, A. I. Orlova[a], A. V. Nokhrin[a], D. A. Mikhailov[a], M. S. Boldin[a], N. V. Sakharov[a], O. A. Belkin[a], E. A. Lantsev[a], M. G. Tokarev[a], and V. N. Chuvil'deev[a]

[a] *Nizhny Novgorod National Research University, Nizhny Novgorod, 603950 Russia*

**e-mail: ekaterina.potanina@list.ru*

Received May 18, 2018; revised July 9, 2018; accepted August 15, 2018

Abstract—Fine-grained $SrWO_4$ and $NaNd(WO_4)_2$ ceramics with the scheelite structure having high relative densities (99 and 95.8%), which can appear candidate matrices for radioactive waste (RAW) management, are prepared by spark plasma sintering (SPS). The phase identity of the ceramics is determined by X-ray powder diffraction; their microstructure is studied by X-ray photoelectron spectroscopy. The tungstates under study are sintered at rather low temperatures (580–665°C). The intensity of compaction of the tungstates at the early sintering stage is determined by the degree of powder agglomeration. The activation energy of fine-grained scheelite ceramics at high temperatures corresponds with the activation energy of grain-boundary oxygen diffusion.

Keywords: ceramics, density, diffusion, activation energy, spark plasma sintering

DOI: 10.1134/S0036023619030161

INTRODUCTION

Now mineral-like compounds are among the most promising materials for immobilizing highly active components of radioactive waste (RAW) [1–4]. Compounds having the structures of monazite [5–7], kosnarite (NZP) [8–10], langbeinite [9, 11], and some other natural minerals are well characterized. Ceramic materials with the scheelite structure are characterized not so well, although recently there has been an increased interest to them [12–16].

Natural scheelite is $CaWO_4$, in which Ca^{2+} can partially or completely be substituted by Sr^{2+}, Ba^{2+}, Cu^{2+}, Mn^{2+}, Cd^{2+}, Pb^{2+}, Cr^{3+}, Fe^{3+}, Ln, Nb^{5+}, or Ta^{5+} and W^{6+} can be substituted by Ge^{4+}, V^{5+}, Mo^{6+}, I^{7+}, or Re^{7+} [17, 18]. Isostructural scheelite-like compounds can contain elements whose isotopes are present in radiochemical technologic waste [17]. Most promising of them are solid solutions of cerium, uranium, plutonium, and americium tungstates [19–21]. An important feature of the scheelite tungstates is their ability to form upon precipitation from alkali chloride melts and a high chemical resistance to them [22, 23]. This is important in the development of methods for the management of RAW from pyrochemical MOX-fuel regeneration technology, when it is necessary to ensure a high stability of materials to the LiCl–KCl chloride melts [23] used in spent nuclear fuel recycling.

Note that the general task of materials design for RAW immobilization is to form a high-density structure in sintered materials, which, all other things being equal, would allow for a high hydrolytic and radiation resistance of ceramics.

Most ceramics based on compounds with the scheelite structure are prepared by cold pressing followed by annealing in vacuo or in air. Sintering temperatures differ depending on ceramic composition, but sintering times are similar, on the order of several hours. For example, $Ca_{1-x}Y_xCeNbWO_8$ ($x = 0$, 0.05, 0.1, 0.15) powders were sintered at 1200°C for up to 9 h [24]. $Na_{0.5}La_{0.5}MoO_4$ and $Ca_{1-x}Bi_xW_{1-x}V_xO_4$ ($x =$ 0.1, 0.2, 0.3, 0.4, 0.5) ceramic samples were prepared in 2 h at a sintering temperature of 789 and 950°C, respectively [25, 26]; the maximal relative density was 96%.

Spark plasma sintering (SPS) technology is of great interest as a variant ceramics sintering process; the underlying idea of this technology is a high-rate (up to 2500°C/min) heating of the material by passing high-amperage (up to 5000 A) millisecond current pulses through a mold containing the powder to be sintered in vacuo or under an inter atmosphere with the simultaneous pressure application. SPS technology combines a set of factors that provide a positive effect to accelerate the sintering process: ultra-high sintering rates, vacuum or an inert atmosphere, application of pressure with its value changing directly during sintering, the tenability of the heating rate at various sintering stages, the implementation of stepped sintering

modes, and others [27–31]. As a result of this, the SPS ceramics have high densities, thermal stability, and good physicomechanical properties [32–34]. Now many researches treat SPS as one of the most promising methods for manufacturing ceramics intended for nuclear power production [35–38], despite the fact that the high-rate sintering mechanisms of fine-grained ceramics yet remain not understood to the fullest extent [30, 39–41].

he goal of the work is to prepare promising tungstates containing neodymium and strontium by the SPS method, study the features of high-rate ceramics sintering, and study the structure and properties of $SrWO_4$ and $NaNd(WO_4)_2$, where Nd and Sr imitate minor actinides, for example, americium Am, and nuclear fission products (rare-earth components and strontium-90).

EXPERIMENTAL

Tungstate powders were prepared by coprecipitation from aqueous solutions. Ammonium tungstate $(NH_4)_4W_5O_{17} \cdot 2.5H_2O$ was dissolved in distilled water at 80°C under constant stirring. After ammonium tungstate dissolved completely, strontium, sodium, and neodymium nitrates were added. The suspensions were stirred for 30 min with a magnetic stirrer, then dried at 90 (for 12 h) and 120°C (for 2 h), mechanically dispersed for 10 min, and annealed successively at 800, 900, 1000, and 1100°C in a SNOL-1 625/11-43 air furnace for 10 h with intermittent dispersion at each stage. The temperature maintenance accuracy was ±5°C.

Ceramics were sintered on a Dr. Sinter model SPS-625 (SPS Syntex). The temperature was brought to 770°C at 30°C/min in vacuo (6 Pa) under uniaxial stress of 75 MPa. The samples were not exposed at the sintering temperature ($\tau = 0$). The sintering temperature for samples of 12 mm in diameter was measured by a Chino IR-AH pyrometer, which was focused on the surface of the graphite mold. The contribution from the thermal expansion of the machine–sample system in constructing temperature-dependent shrinkage (L) and shrinkage rate (S) plots was taken into account in accordance with the approach described in [33]. The temperature measurement accuracy was ±10°C; the pressure maintenance accuracy was ±0.1 MPa.

The functional composition of the compounds was investigated by IR spectroscopy on a Shimadzu FTIR-8400S spectrophotometer at room temperature in the frequency range 400–4000 cm^{-1}.

X-ray powder diffraction experiments were carried out on a Shimadzu LabX XRD-6000 powder diffractometer (CuK_α radiation, $2\theta = 10°–50°$, scan rate: 2 deg/min). Unit cell parameters were calculated from the X-ray powder diffraction data in Powder Diffraction Phase Analysis PhasAnX software (to determine diffraction peak positions) and KRIST software (to calculate the unit cell parameters).

Microstructures of powders and ceramics were studied on a Jeol JSM-6490 scanning electron microscope (SEM) equipped with an Oxford Instruments INCA 350 energy-dispersive microanalyzer. The densities (ρ) of sintered samples were measured by hydrostatic weighing in distilled water using a Sartorius CPA 225D balance. The accuracy was ±0.01 g/cm^3.

RESULTS AND DISCUSSION

The obtained materials were while (Sr-containing) or dark lilac (Nd-containing) agglomerated powders. The packing density of $SrWO_4$ powders in agglomerates was far lower than for $NaNd(WO_4)_2$ powders (Figs. 1a, 1b). The powders had edged shapes. The particle size distributions of the powders are nonuniform: the composites have both coarse particles, averaging to 10 μm, and ultrafine particles with sizes less than 1 μm (Figs. 1c, 1d).

The samples used for IR spectroscopic studies were annealed at 800°C and then stored under air. The IR spectrum of a $NaNd(WO_4)_2$ sample (Fig. 2, curve *2*) features absorption bands at 3388 cm^{-1}, corresponding to the H–O stretching vibrations of hydrate surface layers, and bands at 1616 and 1384 cm^{-1}, relating to the H–O–H bending vibrations of hydrate water molecules. The band in the region 2348 cm^{-1} relates to the stretching vibrations of carbon dioxide molecules. The range of IR frequencies less than 1000 cm^{-1} relates to the characteristic vibrations of W–O. The band lying at 427 cm^{-1} relates to the WO_4 bending vibrations, the absorption bands at 932 and 844 cm^{-1} relate to the stretching vibrations of tungstate tetrahedra, and the bands at 810 and 721 cm^{-1} to the antisymmetrical stretching vibrations. Both water of hydration and carbon dioxide can be sorbed on the material during storage of as-annealed samples.

The results of X-ray diffraction experiments show that $SrWO_4$ and $NaNd(WO_4)_2$ crystallize in scheelite structure, space group $I4_1/a$ (ICDD PDF #08-0490 and #79-1119, respectively) (Fig. 3). The unit cell parameters of the compounds had the following values: for $SrWO_4$, $a = b = 5.4293 \pm 0.0005$ Å, $c = 11.9781 \pm 0.0017$ Å, $\alpha = \beta = \gamma = 90°$; for $NaNd(WO_4)_2$, $a = b = 5.2954 \pm 0.0006$ Å, $c = 11.4930 \pm 0.0015$ Å, $\alpha = \beta = \gamma = 90°$. The theoretical densities (ρ_{th}) of $SrWO_4$ and $NaNd(WO_4)_2$ ceramics were 6.3086 and 6.8290 g/cm^3, respectively.

Ceramic sintering diagrams are shown in Fig. 4. One can see that tungstate powders are sintered at rather low temperatures. The temperature corresponding to the highest sintering rate, T_1, is 580–600 and 645–665°C for $SrWO_4$ and $NaNd(WO_4)_2$ ceramics, respectively. Noteworthy, the densening onset temperature

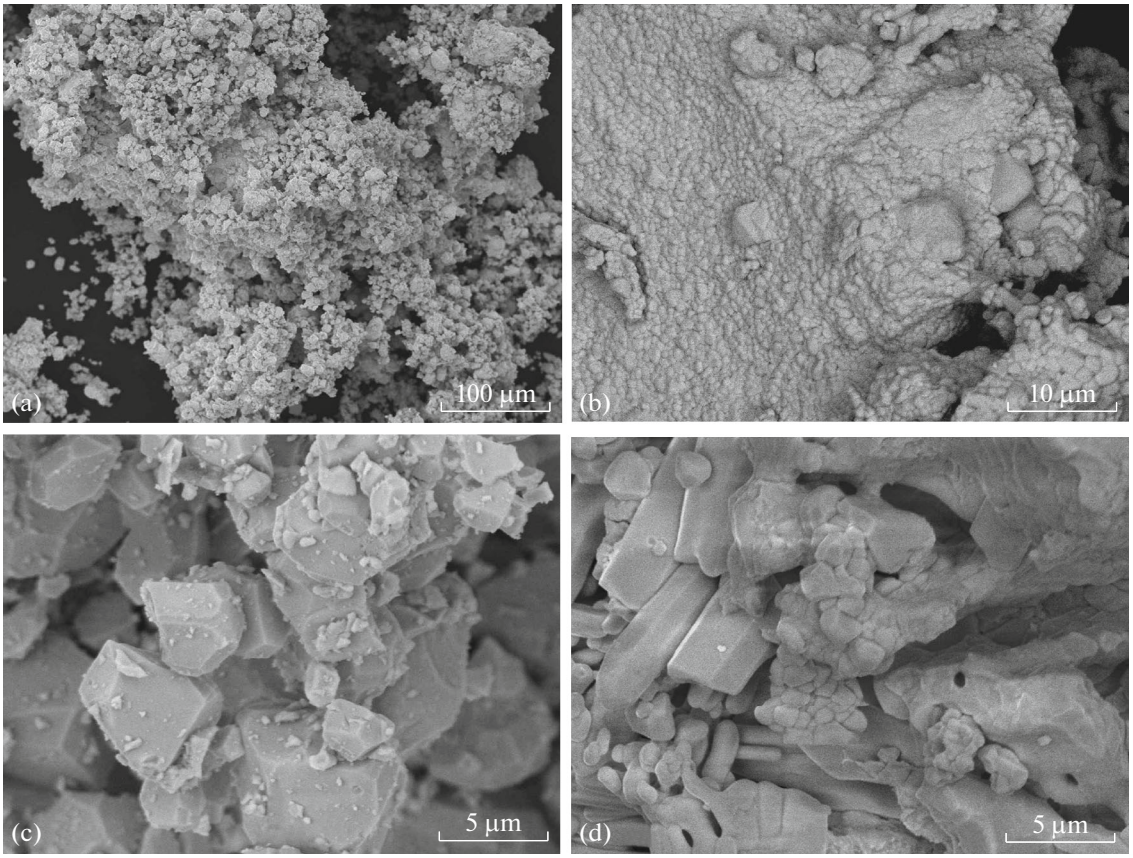

Fig. 1. Images of (a, c) $SrWO_4$ and (b, d) $NaNd(WO_4)_2$ powder structures under various magnifications.

for $SrWO_4$ powders (240–250°C) is lower than for $NaNd(WO_4)_2$ powders (585–600°C); the likely reason for this is the denser packing in $NaNd(WO_4)_2$ agglomerated powders (Fig. 1b). This leads to more intense sintering of $NaNd(WO_4)_2$ ceramics, although the maximal shrinkage L_{max} for $SrWO_4$ powders is greater (L_{max} = 0.72 mm) than for $NaNd(WO_4)_2$ powders (L_{max} = 0.53 mm).

The density of the manufactured $SrWO_4$ and $NaNd(WO_4)_2$ ceramics is 99.0 and 95.8%, respectively. The phase composition of the ceramics

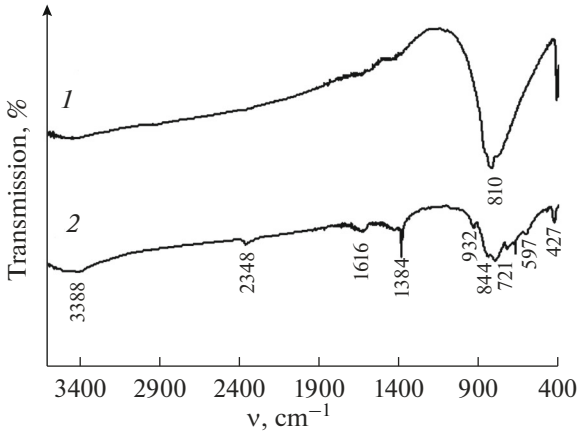

Fig. 2. IR spectra of (*1*) $SrWO_4$ and (*2*) $NaNd(WO_4)_2$ samples.

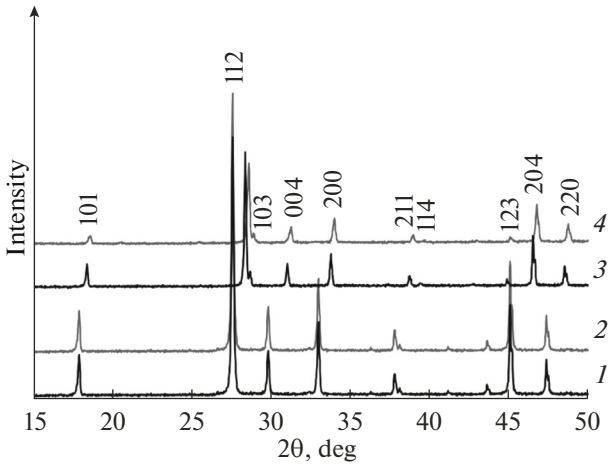

Fig. 3. X-ray diffraction patterns of (*1*, *3*) powders and (*2*, *4*) ceramics of (*1*, *2*) $SrWO_4$ and (*3*, *4*) $NaNd(WO_4)_2$.

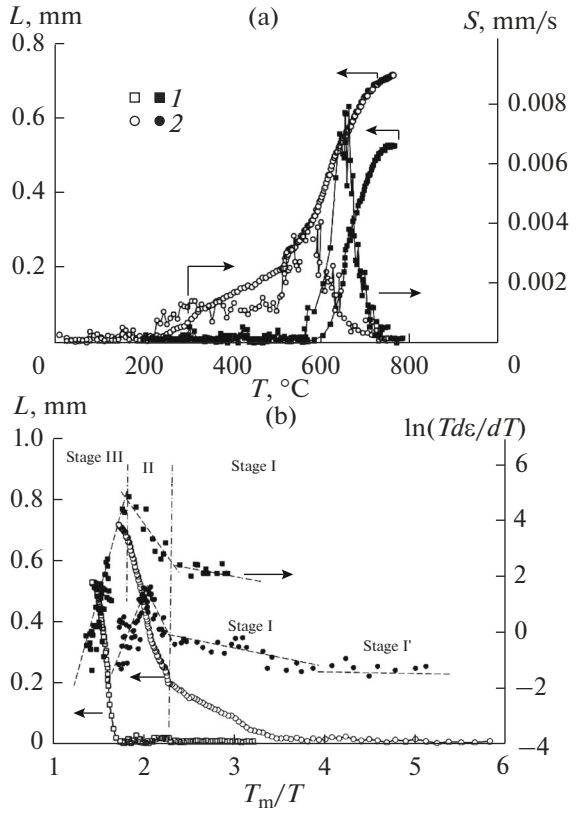

Fig. 4. Sintering diagrams of (*1*) $SrWO_4$ and (*2*) $NaNd(WO_4)_2$ ceramics: (a) shrinkage L (light markers) and shrinkage rate S (dark markers) versus heating temperature (T) and (b) L–T_m/T plots (light markers) and $\ln(Td\varepsilon/dT)$–T_m/T (dark markers).

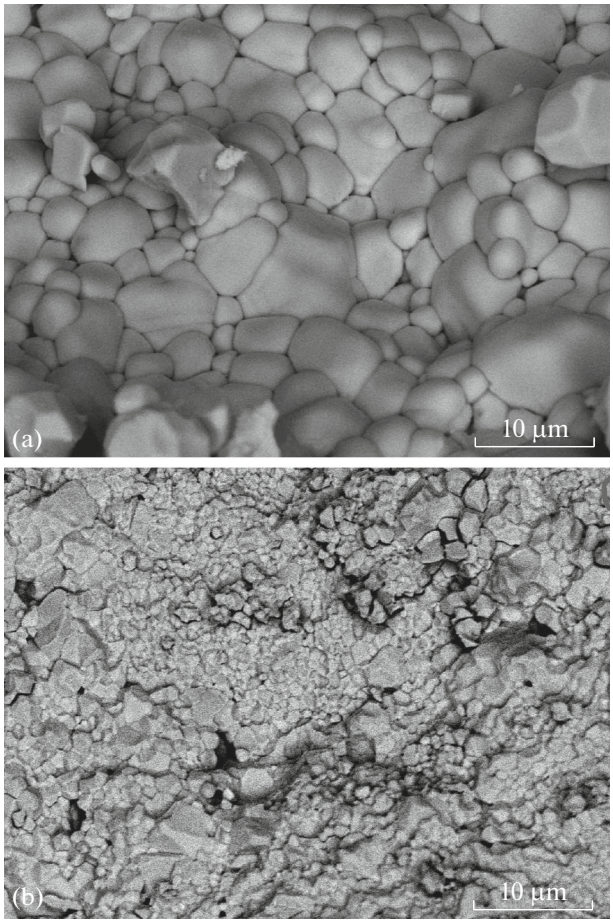

Fig. 5. Micrographs of (a) $SrWO_4$ and (b) $NaNd(WO_4)_2$ ceramics. SEM images of fractures.

remained unchanged after SPS (Fig. 3), indicating a high thermal stability of the crystal structure of the prepared compounds.

The results of electron-microscopic studies show that the ceramics have high-density fine-grained structures (Fig. 5). Most grains of the $SrWO_4$ ceramics have sizes from 4 to 10 μm; the $NaNd(WO_4)_2$ ceramics have grain sizes of ~1–2 μm. Coarse grains are observed in both ceramic structures, indicating their abnormal growth in the course of sintering. Single coarse tungstate particles retaining their edged shapes are observed on fractures (Fig. 6), which testifies to the incompleteness of their sintering with the main fine-grained ceramic matrix. The volume fraction of such large particles in the ceramics fracture does not exceed 1–2%.

Let us analyze the features of the sintering kinetics of fine-grained tungstates powders at various heating stages.

A preliminary analysis of the dominant diffusion mechanisms that occur at the early stages of sintering with continuous heating can be carried out using the Young–Culter and Dorn models [42]; these models were developed to analyze nonisothermal sintering modes. In terms of this approach, the effective activation energy of sintering mQ_s (where $m = 1/2$ for bulk diffusion in the crystal lattice and $m = 1/3$ for grain-boundary diffusion [42–44]) under continuous heating can provisionally be estimated from the slope of the shrinkage versus temperature in semi-logarithmic coordinates $\ln(Td\varepsilon/dT)$–T_m/T [45] (Fig. 4), where $\varepsilon = L/L_0$, L_0 is initial sample height, and T_m is melting temperature of the ceramics (T_m = 1808 K for $SrWO_4$ [46], and T_m = 1508 K for $NaNd(WO_4)_2$ [47]).

The analysis shows that the early stage of the density versus heating temperature plot $\ln(Td\varepsilon/dT)$–T_m/T can be divided into two temperature ranges, each being characterized by its own effective activation energy mQ_s, namely, stage I with a low activation energy $mQ_{s(1)} \sim 1–1.5\ kT_m$ and stage II with the activation energy $mQ_{s(2)} \sim 3.5–4.0\ kT_m$ for $SrWO_4$ and ~9.5–10 kT_m for $NaNd(WO_4)_2$, where k is Boltzmann's constant (Fig. 3). At higher sintering temperatures, the $\ln(Td\varepsilon/dT)$–T_m/T slope becomes negative (stage III), so the Dorn method becomes useless in this temperature range and other approaches need to be used to

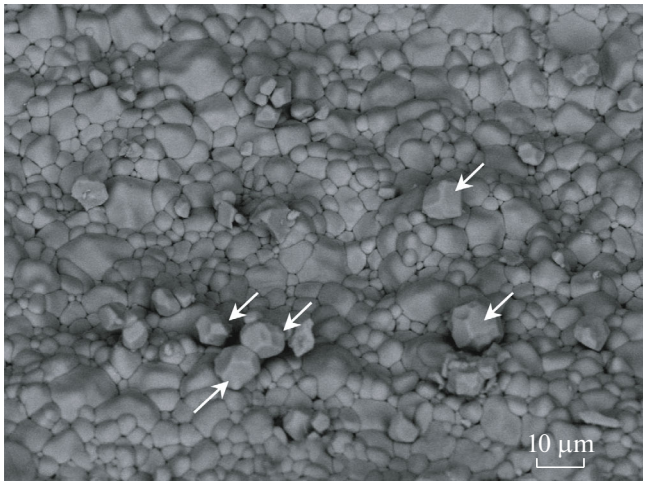

Fig. 6. Microstructure of sintered $SrWO_4$ ceramics. The SEM image of fracture. Coarse particles that retain edged shapes are marked with arrows.

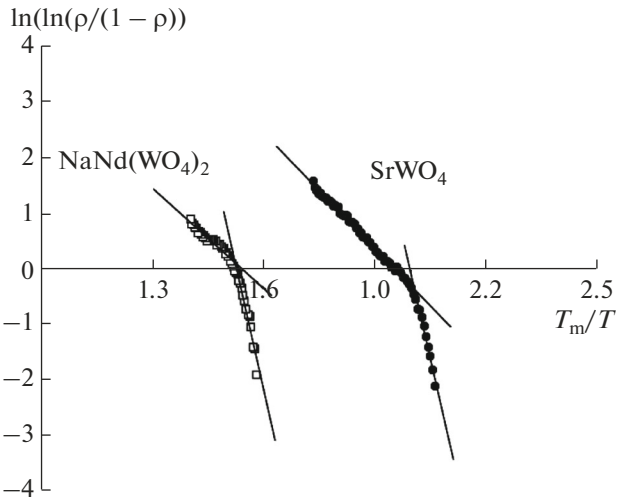

Fig. 7. Density versus sintering temperature in double logarithmic coordinates $\ln(\ln[(\rho_{exp}/\rho_{th})/(1 - \rho_{exp}/\rho_{th})])-T_m/T$ ($\rho = \rho_{exp}/\rho_{th}$).

assess the effective energy of sintering. Noteworthy, the staged temperature-dependent compaction (stage I: a low activation energy[1], stage II: a high activation energy, and stage III: a negative slope) discovered in the study corresponds with the published results [44], and confirms the correctness of the approach.

In accordance with the approach described in [32, 34, 48], the activation energies of sintering Q_s for stages II and III can be derived from the slope of the $\rho/\rho_{th}(T)$ plot in the double logarithmic coordinates: $\ln(\ln[(\rho/\rho_{th})/(1 - \rho/\rho_{th})])-T_m/T$. Since the diameter of a sintered sample is dictated by the inner diameter of the mold and remains virtually unchanged upon heating, the change in shrinkage may be equated to the change in powder density. For the sake of a comparison analysis of sintering kinetics, L/L_0-T plots were transformed to densening diagrams $\rho/\rho_{th}-T$ (the details of transformation of the temperature-dependent shrinkage into temperature-dependent density can be found elsewhere [32, 34, 48]). The correctness of $\rho/\rho_{th}-T$ calculations was checked by comparing the density corresponding to the maximal shrinkage with the experimentally measured value ρ_{max}.

The analysis in terms of the above-described approach showed that $L(T)$ plots in the range of the heating temperatures corresponding to stages II and III in the double logarithmic coordinates $\ln(\ln[(\rho/\rho_{th})/(1 - \rho/\rho_{th})])-T_m/T$ for $SrWO_4$ and $NaNd(WO_4)_2$, can be interpolated by two straight lines with different slopes (Fig. 7). The activation energy of sintering $Q_{s(2)}$, determined from the $\ln(\ln[(\rho/\rho_{th})/(1 - \rho/\rho_{th})])-T_m/T$ slope, at stage II was found to be higher than the activation energy of sintering at higher temperatures, $Q_{s(3)}$, at the last sintering stage (stage III).

The analysis shows that the activation energy of sintering $Q_{s(2)}$ is 10–12 kT_m (~150–180 kJ/mol) and ~16–18 kT_m (~200–226 kJ/mol), respectively, for $SrWO_4$ and $NaNd(WO_4)_2$ powders. The values calculated for the activation energy $Q_{s(2)}$ using two approaches are in agreement with each other for $m = 1/3$, which corresponds to grain-boundary diffusion.

The $SrWO_4$ scheelite structure, which is formed by anionic (WO_4) and cationic (SrO_8) groups, is a framework [49, 50]. A Sr atom is surrounded by eight O atoms to form a dodecahedron, and a W atom is surrounded by four O atoms to form a tetrahedron. Eight-vertice polyhedra SrO_8 are linked via shared edges, where each SrO_8 polyhedron is fused with four neighboring ones. Tungstate $NaNd(WO_4)_2$ has a similar structure, with the only difference that strontium atoms are substituted by Na and Nd [51].

The scheelite crystal structure greatly complicates the analysis of diffusion data. The W–O atomic bond energy is known to be far higher than the A–O (where A = Sr, Nd, Na, Ca, etc.) bond energy [45]. In particular, the W–O bond energy in scheelite $CaWO_4$ is 610 kJ/mol, while the Ca–O bond energy is as low as 130 kJ/mol [45]. This implies that diffusion in scheelite occurs via the dissociation of A–O bonds and oxygen diffusion in the scheelite crystal structure [45].

Analysis of the literature data shows that the activation energy of oxygen diffusion in strontium oxide varies from 263 to 445 kJ/mol [52–54]. The activation

[1] According to [44], at stage I, individual isolated particles are sintered with agglomerates that have been formed in the course of synthesis with simultaneous rearrangement of particles in these agglomerates. The dominant compaction mechanism at this stage is surface diffusion, and this explains the low compaction intensity at this stage.

energy of tungsten atoms in the $CaWO_4$ crystal lattice is 230–280 kJ/mol [45]. According to [45], the activation energy of tungsten grain-boundary diffusion in $CaWO_4$ ceramics is 75 kJ/mol, and the activation energy of calcium grain-boundary diffusion is 100 kJ/mol [45].

Neiman [45] analyzing the Nernst–Einstein equation observes that, in the crystal lattices of scheelite tungstates and molybdates, the activation energy of scheelite oxygen is close to the activation energy of metal atoms (regardless of the type of diffusing metal atom), despite an appreciable difference between the pre-exponential factors (diffusion coefficients D_0). This inference corresponds with the analysis of grain-boundary diffusion features in ceramics [55–57].

Thus, we may conclude the following: the sintering intensity for fine-grained scheelite ceramics at elevated temperatures is controlled by the intensity of grain-boundary oxygen diffusion. This conclusion is indirectly confirmed by the fact that the sintering of ceramics occurs at relatively low temperatures (~$0.48–0.50T_m$ for $SrWO_4$ and ~$0.62–0.65T_m$ for $NaNd(WO_4)_2$), at which temperatures the bulk diffusion intensity is low [57–61].

The more intense grain growth in $SrWO_4$ ceramics (Fig. 5a) may be explained by the lower activation energy of grain-boundary diffusion in this ceramics and by the more compact packing of powders in agglomerates, thereby the smaller initial pore size between individual scheelite particles. In turn, this results in shortening of the characteristic time of diffusion pore resorption and thereby a more early grain growth onset during sintering.

CONCLUSIONS

Fine-grained $SrWO_4$ and $NaNd(WO_4)_2$ ceramics with the scheelite structure having high relative densities (99 and 95.8%) have been obtained by SPS. The optimal ceramics sintering rate corresponding to the maximal shrinkage rate, is low and amounts to ~$0.48–0.65T_m$ at the heating rate 30°C/min.

The compaction intensity of tungstate powders at low temperatures is due to the sliding of individual particles relative to each other in agglomerates, and the degree of compaction at this stage significantly depends on the packing density of powders in agglomerates of the synthesized powders.

The sintering activation energy of fine-grained tungstates at high temperatures corresponds to the activation energy of grain-boundary oxygen diffusion in the scheelite crystal structure. The finer grain structure in $NaNd(WO_4)_2$ ceramics is due to the higher activation energy of grain-boundary diffusion in $NaNd(WO_4)_2$ ceramics than in $SrWO_4$.

ACKNOWLEDGMENTS

This study was supported by the Russian Scientific Foundation (project no. 16-13-10464).

REFERENCES

1. G. J. McCarthy and M. T. Davidson, Bull. Am. Ceram. Soc. **54**, 782 (1975).
2. W. Lutze and R. C. Ewing, *Radioactive Waste Forms for the Future* (North-Holland, 1988).
3. B. E. Burakov, M. I. Ojovan, and W. E. Lee, *Crystalline Materials for Actinide Immobilization. Materials for Engineering* (Imperial College Press, London, 2010), Vol. 1.
4. C. M. Jantzen, W. E. Lee, and M. I. Ojovan, *Radioactive Waste Management and Contaminated Site Clean-Up. Processes, Technologies and International Experience* (Woodhead, Oxford/Cambridge/Philadelphia/New Delhi, 2013).
5. S. N. Achary, S. Bevara, and A. K. Tyagi, Coord. Chem. Rev. **340**, 266 (2017). doi 10.1016/j.ccr.2017.03.006
6. Y. Arinicheva, N. Clavier, and S. Neumeier, J. Eur. Ceram. Soc. **38**, 227 (2018). doi 10.1016/j.jeurceramsoc.2017.08.008
7. S. Neumeier, Yu. Arinicheva, Y. Ji, et al., Radiochim. Acta **105**, 961 (2017). doi 10.1515/ract-2017-2819
8. A. Ananthanarayanan, R. D. Ambashta, and V. Sudarsan, J. Nucl. Mater. **487**, 5 (2017). doi 10.1016/j.jnucmat.2017.01.054
9. A. I. Orlova, *Structural Chemistry of Inorganic Actinide Compounds* (Elsevier, Amsterdam, 2007).
10. D. J. Gregg, I. Karatchevtseva, G. J. Thorogood, et al., J. Nucl. Mater. **446**, 224 (2014). doi 10.1016/j.jnucmat.2013.11.048
11. S. P. Kumar and B. Gopal, J. Alloys Compd. **657**, 422 (2016). doi 10.1016/j.jallcom.2015.10.088
12. G. Canu, V. Buscagila, C. Ferrara, et al., J. Alloys Compd. **697**, 392 (2017). doi 10.1016/j.jallcom.2016.12.111
13. I. L. Shukaev, E. A. Mukhanova, and T. G. Lupeiko, Solid State Ionics **298**, 51 (2016). doi 10.1016/j.ssi.2016.10.018
14. M. Paitkowska and E. Tomaszewicz, J. Therm. Anal. Calorim. **126**, 111 (2016). doi 10.1007/s10973-016-5499-2
15. J. Cheng and J. He, Mater. Lett. **209**, 525 (2017). doi 10.1016/j.matlet.2017.08.094
16. P. Mogilevsky, T. A. Parthasarathy, and M. D. Petry, Acta Mater. **52**, 5529 (2004). doi 10.1016/j.actamat.2004.08.022
17. D. Errandonea and F. J. Manjon, Prog. Mater. Sci. **53**, 711 (2008). doi 10.1016/j.pmatsci. 2008.02.001
18. V. A. Morozov, A. V. Mironov, B. I. Lazoryak, et al., J. Solid State Chem. **179**, 1183 (2006). doi 10.1016/j.jssc.2005.12.041
19. R. H. D. Passos, M. Arab, C. P. de Souza, and Ch. Leroux, Acta Crystallogr., Sect. B **73**, 466 (2017). doi 10.1107/S2052520617002827

20. A. Tabuteau and M. Pages, J. Inorg. Nucl. Chem. **42**, 401 (1988). doi 10.1016/0022-1902(80)80015-7
21. A. Tabuteau and M. Pages, J. Solid State Chem. **26**, 153 (1978).
22. A. Packter, Cryst. Res. Technol. **17**, 377 (1982). doi 10.1002/crat.2170170323
23. E. Potanina, A. Orlova, and M. Kalenova, Proceedings of the XVII Radiochemical Conference, Marianske Lazne, Czech Republic (2014), p. 418
24. B. Zhang, Q. Zhao, Ch. Zhao, and A. Chang, J. Alloys Compd. **698**, 1 (2017).
25. B. Dingyaominn, Ceram. Int. **39**, 1555 (2013).
26. H. Xi, D. Zhou, H. Xie, and W. Li, Mater. Lett. **142**, 221 (2015).
27. M. Tokita, in *Handbook of Advanced Ceramics* (Academic Press, Amsterdam, 2013), p. 1149. http://dx.doi.org/10.1016/B978-0-12-385469-8.00060-5.
28. C. Mamiere, G. Lee, and E. A. Olevsky, Sci. Repts **7** (1), 15071 (2017). doi 10.1038/s41598-017-15365-x
29. V. N. Chuvil'deev, D. V. Panov, M. S. Boldin, et al., Acta Astronaut. **109**, 172 (2015) http://dx.doi.org/10.1016/j.actaastro.2014.11.008.
30. Z. A. Munir and D. V. Quach, J. Am. Ceram. Soc. **94**, 1 (2011). https://doio.org/10.1111/j.1551-2916.2010.04210.x
31. D. Dudina and A. K. Mukherjee, J. Nanomater. **11**, 625218 (2013). doi 10.1155/2013/625218
32. E. Potanina, L. Golovkina, A. Orlova, et al., J. Nucl. Mater. **473**, 93 (2016). doi 10.1016/j.jnucmat.2016.02.014
33. V. N. Chuvil'deev, A. V. Nokhrin, G. V. Baranov, et al., Nanotechnol. Russia **8**, 108 (2013). doi 10.1134/S1995078013010047
34. V. N. Chuvil'deev, Yu. V. Blagoveshchenskiy, A. V. Nokhrin, et al., J. Alloys Compds **708**, 547 (2017). doi 10.1016/j.jallcom.2017.03.035
35. H. R. Williams, H. Ning, M. J. Reece, et al., J. Nucl. Mater. **433**, 116 (2013). doi 10.1016/j.jnucmat.2012.09.030
36. R. C. O'Brien, R. M. Ambrosi, N. P. Bannister, et al., J. Nucl. Mater. **393**, 108 (2009). doi 10.1016/j.jnucmat.2009.05.012
37. K. D. Johnson and D. A. Lopes, J. Nucl. Mater. **503**, 75 (2018). doi 10.1016/j.jnucmat.2018.02.041
38. H. J. Ryu, Y. W. Lee, S. I. Cha, and S. H. Hong, J. Nucl. Mater. **352**, 341 (2006). doi 10.1016/j.jnucmat.2006.02.089
39. D. V. Dudina and B. B. Bokhonov, Adv. Powder Technol. **28**, 641 (2017). doi 10.1016/ j.apt.2016.12.001
40. V. N. Chuvil'deev, M. S. Boldin, A. V. Nokhrin, and A. A. Popov, Acta Astronaut. **135**, 192 (2017). doi 10.1016/j.actaastro.2016.09.002
41. D. V. Dudina, A. G. Anisimov, V. I. Mali, et al., Mater. Lett. **144**, 168 (2015). doi 10.1016/j.matlet.2015.01.042
42. W. S. Young and I. B. Culter, J. Am. Ceram. Soc. **53**, 659 (1970). doi 10.1111/j.1151-2916.1970.tb12036.x
43. J. J. Bacmann and G. Cizeron, J. Am. Ceram. Soc. **51**, 209 (1968). doi 10.1111/j.1151-2916.1968.tb11874.x
44. KumarA. K. Nanda, M. Watabe, and K. Kurokawa, Ceram. Int. **37**, 2643 (2011). doi 10.1016/j.ceramint.2011.04.011
45. A. Ya. Neiman, Solid State Ionics **83**, 263 (1996). doi 10.1016/0167-2738(95)00247-2
46. R. C. Ropp, *Encyclopedia of the Alkaline Earth Compounds* (Elsevier, 2013).
47. S. Oishi and I. Tate, Chem. Lett., 1449 (1980).
48. V. N. Chuvil'deev, M. S. Boldin, Ya. G. Dyatlova, et al., Inorg. Mater. **51**, 1047 (2015). doi 10.1134/S0020168515090034
49. E. Gurmen, E. Daniels, and J. S. King, J. Chem. Phys. **55**, 1093 (1971). doi 10.1063/1.1676191
50. H. Li, G. Hong, and S. Yue, J. Chin. Rare Earth Soc. **8**, 37 (1990).
51. J. R. Thornton, W. D. Fountain, G. W. Flint, and T. G. Crow, Appl. Opt. **8**, 1087 (1969). doi 10.1364/AO.8.001087
52. V. N. Chuvil'deev and E. S. Smirnova, Phys. Solid State **58**, 1487 (2016). http://dx.doi.org/10.1134/S1063783416070118.
53. S. Mrowec, React. Solids **5**, 241 (1988). doi 10.1016/0168-7336(88)80025-1
54. A. R. Andrievskii and I. I. Spivak, *Strength of High-Melting Compounds and Materials on Their Base: A Reference Book* (Metallurgiya, Chelyabinsk, 1989) [in Russian].
55. A. V. Nokhrin, Tech. Phys. Lett. **38**, 630 (2012). http://dx.doi.org/10.1134/S1063785012070073.
56. J. Pelleg, *Diffusion in Ceramics* (Springer. 2016). http://dx.doi.org/10.1007/978-3-319-18437-1.
57. G. Erdelyi and D. L. Beke, Diffusion in Non-Metallic Solids (Part 1). Landolt-Börnstein: Group III Condensed Mater., 33B1 (1991).
58. R. L. Coble, J. Appl. Phys. **32**, 787 (1961). doi 10.1063/1.1736107
59. R. L. Coble, J. Appl. Phys. **32**, 793 (1961). doi 10.1063/1.1736108
60. W. D. Kingery, H. K. Bowen, and D. R. Uhlmann, *Introduction in Ceramics*, Second Ed. (Wiley, New York, 1976).
61. M. N. Rahaman, *Ceramic Processing and Sintering* (Marcel Dekker, New York, 2003).

Translated by O. Fedorova